

## Effects of Second Thermal Cycles on Microstructure and CO<sub>2</sub> Corrosion Behavior of X80 Pipeline Steel

Shi chuanwei\*, Zhang yuanbin, Liu peng, Xie yueliang

School of Material Science and Engineering, Shandong Jianzhu University, Jinan 250101, China

\*E-mail: [shichuanwei@sdjzu.edu.cn](mailto:shichuanwei@sdjzu.edu.cn)

Received: 7 September 2017 / Accepted: 9 January 2018 / Published: 5 February 2018

---

The effects of the gas metal arc welding (GMAW) thermal cycle on the microstructures and carbon dioxide (CO<sub>2</sub>) corrosion behaviors of X80 pipeline steel and its coarse-grained heat-affected zone (CGHAZ) from submerged arc welding (SAW) were studied. Different microstructural gradients were found to form in the two joints. The CO<sub>2</sub> corrosion resistances of those samples experiencing the SAW thermal cycle were inferior to those not experiencing it because of their relatively coarse microstructures. Two completely different corrosion mechanisms were operative for the base metal (BM) and the heat-affected zones in the electrolyte. The preferential dissolution of the martensite/austenite (M/A) constituents contributed to the presence of pitting and produced an inductive loop in the Nyquist plots and pitting holes in the corrosion morphologies of some of the sample surfaces. More importantly, the corrosion resistance of the intercritical CGHAZ (ICCGHAZ) with a secondary peak temperature between the characteristic austenite formation temperatures, Ac<sub>1</sub> and Ac<sub>3</sub>, was the weakest because of the presence of coarse necklace-shaped M/A constituents and high-carbon martensite.

---

**Keywords:** second thermal cycles; heat-affected zone (HAZ); carbon dioxide (CO<sub>2</sub>) corrosion; M/A constituents

### 1. INTRODUCTION

High-strength low-alloy pipeline steels, such as X70 and X80, which are produced by thermo-mechanical controlled processing, have been used widely in the petroleum industries because of their favorable combination of high strength and good toughness with high efficiency and low cost [1-3]. Welding is known to be an effective and widely used method for fabricating cylindrical pipes with large diameters and for connecting the pipes in field [2]. In conjunction with the development of pipeline steels, welding methods have also been investigated. The microstructure and properties of

welded joints, especially those of the heat-affected zone (HAZ), strongly depend on the applied thermal cycles, which therefore have received considerable attention [4]. According to the peak temperature during the welding thermal cycles, the HAZ can be divided into the subcritical HAZ (SHAZ), intercritical HAZ (ICHAZ), supercritical HAZ (SCHAZ) and coarse-grained HAZ (CGHAZ). In recent years, studies on the effects of second thermal cycles on the microstructure and properties of welded joints, particularly of the CGHAZ, have attracted considerable attention [5-10]. According to the peak temperature in the second thermal cycles, the reheated CGHAZ that is subjected to a second thermal cycles can be divided into the subcritical CGHAZ (SCGHAZ), intercritical CGHAZ (ICCGHAZ), supercritical CGHAZ (SCCGHAZ), and unaltered CGHAZ (UCGHAZ). The ICCGHAZ, in which the peak temperature in the second thermal cycles is between the characteristic austenite formation temperatures,  $A_{c1}$  and  $A_{c3}$ , has the lowest toughness because of the neck-lace shape of the martensite/austenite (M/A) constituents [7, 10]. For the ICCGHAZ, the higher heat input in the first welding thermal cycle and the closer to  $A_{c1}$  of the second peak temperature contribute to the low toughness [6, 7]. In addition, the fatigue crack growth rate was the fastest in ICCGHAZ because of the rapid crack initiation and propagation that occurs via the massive M/A constituents [8]. In general, there are two types of pipeline steel welding: seam welding, which is performed in the pipeline steel factories, and girth welding, which is performed in the field. To ensure economic efficiency and a good weld quality, the welding methods often employed for seam welding and girth welding are respectively submerged arc welding (SAW) with a relatively high heat input and gas metal arc welding (GMAW) with a relatively low heat input. The SAW joint zone, like the other zones in the girth method, also undergoes a second thermal cycle of GMAW, which greatly affects the microstructure and properties.

The corrosion of pipelines, which depends on the internal and external environments, is difficult to predict and control [11, 12], especially in the welded joint. To date, there have been some published papers reporting the corrosion behavior of the HAZ. The HAZ has been shown to be the weak zone in terms of the corrosion resistance because of the microstructural variations and the presence of welding residual stress introduced by the welding thermal cycles [2, 13, 14]. In addition, localized corrosion occurs in the welds because of the galvanic effect among the HAZ, base metal (BM) and welded materials. The failure often occurs in or near the welded joint according to the experience in the field [13]. On the other hand, carbon dioxide ( $CO_2$ ) corrosion, which is inevitable in pipelines and difficult to predict and control, has attracted substantial consideration and attention for several decades [15]. In previous studies, the effects of the temperature, partial pressure, chloride ion and corrosion films on the  $CO_2$  corrosion behavior of carbon steels were examined [15-17]. The localized corrosion of steel was shown to occur in  $CO_2$ -containing corrosive environments and the steel surface was covered by a product scale whose stability was affected by the temperature and immersion time [18]. However, the  $CO_2$  corrosion behavior of welded joints with different microstructures is relatively unknown, as are the effects of a second thermal cycle

The real HAZ is too narrow to study its corrosion resistance, and the welding thermal simulation provides an effective way to obtain a single thermal simulated HAZ specimen with a certain heat input and peak temperature. In this study, welding thermal simulation was used to study the effects of second thermal cycles on the microstructure and corrosion resistance of the CGHAZ in a seam-welded joint in 5.0 wt.% NaCl with saturated  $CO_2$ . Heat inputs of 30 kJ/cm and 10 kJ/cm were

selected to simulate the SAW and GMAW thermal cycles. To compare the results and make them more conclusive, the HAZs that were subjected to only the GMAW thermal cycles were also studied. We believe that the obtained results provide the ability to better predict on the corrosion of pipeline steel.

## 2. EXPERIMENTAL PROCEDURE

### 2.1 Materials

The X80 pipeline steels used in this study were produced by low-alloying and thermo-mechanical controlled processing. The chemical composition (wt.%) was as follows: C 0.046, Si 0.305, Mn 1.76, P 0.007, S 0.001, Al 0.058, Nb 0.079, V 0.008, Ni 0.225, Cr 0.023, Mo 0.226, B 0.00025, Ti 0.015, Ca 0.001, Cu 0.215 and Fe balanced.

### 2.2 Welding thermal simulation

The simulated heat-affected zone (HAZ) and reheated coarse-grained HAZ (CGHAZ) samples were obtained by welding thermal simulation, which was performed using a Gleeble 3500 simulator. The samples that were subjected to submerged arc welding (SAW) thermal cycles and gas metal arc welding (GMAW) are called SAW+GMAW HAZs. The samples not subjected to the SAW thermal cycles can be viewed as experiencing only room temperature (RT) in the first welding thermal cycle and the GMAW thermal cycles. Thus, they are called RT+GMAW HAZs. Schematic diagrams of the simulation are shown in Fig. 1, and the specific parameters are shown in Table 1. Microstructural observation of base metal (BM) and HAZs was carried out by a VHX\_500F KEYENCE optical microscope (OM) after etching with 4% Nital (4 mL nitric acid and 96 mL ethanol) and by an EM-002B transmission electron microscopy (TEM) after twin-jet polishing. Micro-hardness measurements were carried out with a 200 g load and a 15 s loading time, and each sample was tested 20 times to ensure accuracy.

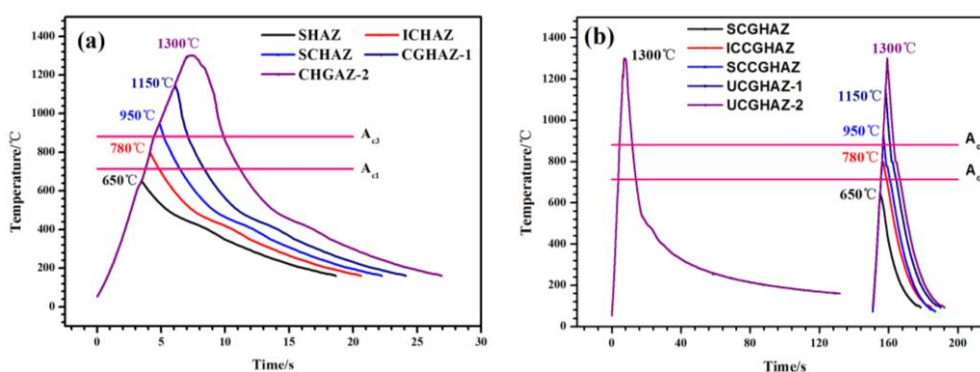


**Figure 1.** Schematic diagrams of the welding thermal cycles for the samples (a) RT+GMAW and (b) SAW+GMAW.

**Table 1.** Specific welding thermal simulation parameters ( $T_p$  and  $E$  represent the peak temperature and heat input, respectively, in the welding process)

		First thermal cycle		Second thermal cycle	
		$T_p$ (°C)	$E$ (kJ/cm)	$T_p$ (°C)	$E$ (kJ/cm)
	BM	--	--	--	--
	CGHAZ	1300	30	--	--
RT-GMAW	SHAZ	--	--	650	10
	ICHAZ	--	--	780	10
	SCHAZ	--	--	950	10
	CGHAZ-1	--	--	1150	10
	CGHAZ-2	--	--	1300	10
SAW-GMAW	SCGHAZ	1300	30	650	10
	ICCGHAZ	1300	30	780	10
	SCCGHAZ	1300	30	950	10
	UCGHAZ-1	1300	30	1150	10
	UCGHAZ-2	1300	30	1300	10

### 2.3 Immersion and electrochemical measurements

The test solution used in this study was 5.0 wt.% NaCl solution with saturated carbon dioxide ( $\text{CO}_2$ ), and the pH and temperature were maintained at 4.3 and 60 °C, respectively. Specimens were machined into a rectangular shape with dimensions of 10 × 10 mm<sup>2</sup> (an area of 1 cm<sup>2</sup>) and sealed with epoxy resin with the end face exposed to the solution. Prior to the immersion measurements, the specimens were ground with 800-grit emery paper, cleaned with acetone, alcohol and distilled water in sequence, dried with cool air, and then mounted in silica gel. The corrosion rate was determined by the weight loss. In addition, a three-electrode electrochemical cell system was employed with the studied material as the working electrode, a platinum plate as the counter electrode, and a saturated calomel electrode (SCE) of +0.241 V<sub>SHE</sub> as the reference electrode. The potentials used in this study were referenced to the SCE. The open circuit potential (OCP) measurements were carried out for 8 days (d). The electrochemical impedance spectroscopy (EIS) measurements were carried out with a 10 mV amplitude and frequencies from 0.01 Hz to 100 kHz. The immersion experiments were performed for 1, 2, 4, 6 and 8 d, after which the weight loss was calculated. In addition, after immersion for 8 d, the corroded region was cut to observe the corrosion morphologies by a JSM-6480 LA scanning electron microscope (SEM).

## 3. RESULTS

### 3.1 Microstructural evolution

#### 3.1.1 Microstructure of the as-received BM and the CGHAZ of SAW

The X80 pipeline steel used in this study is a dual-phase steel, and its microstructure mainly consists of polygonal ferrite (PF) with fine grains of approximately 3.6 μm and granular bainite (GB), in which the M/A constituents are present as a secondary phase (Fig. 2a). As shown in Fig. 2b, the

microstructure of the CGHAZ of SAW is mainly GB with coarse prior austenite grain boundaries, which can be seen clearly. The M/A constituents, present as granules, are parallel to each other in one austenite grain, but not in different prior austenite grains.

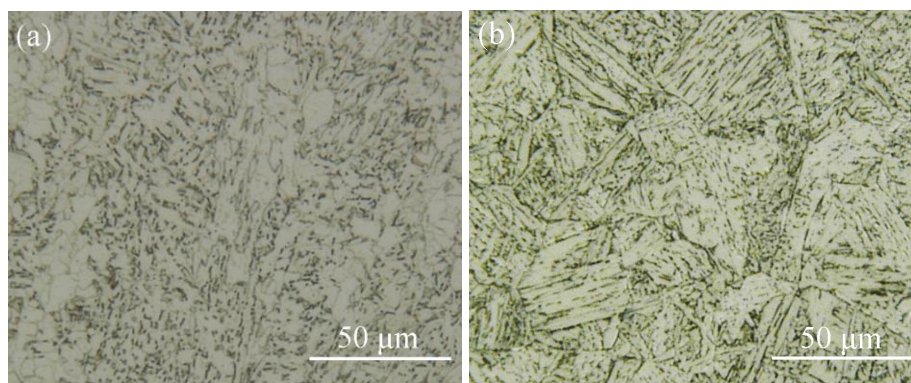


**Figure 2.** OM images of the microstructure of (a) the BM and (b) the CGHAZ of SAW.

### 3.1.2 Microstructural evolution in the simulated HAZs

The resulting microstructures of simulated HAZs experiencing the RT+GMAW and SAW+GMAW thermal cycles are shown in Figs. 3 and 4, respectively. In addition, the micro-hardness is shown in Fig. 5. The main microstructural characteristics of the BM and HAZs are summarized in Table 2.

According to the empirical equations proposed by K. Andrews [19], the characteristic austenite formation temperatures, called the  $Ac_1$  and  $Ac_3$  temperatures, for the X80 steel can be predicted as follows:

$$Ac_1(^{\circ}C)=723-10.7w(Mn)-3.9w(Ni)+29w(Si)+16.7w(Cr)+290w(As)+6.38w(W) \quad (1)$$

$$Ac_3(^{\circ}C)=910-230w(C)^{0.5}-15.2w(Ni)+44.7w(Si)+104w(V)+31.5w(Mo)+13.1w(W) \quad (2)$$

where  $w$  represents the mass percent (%). The X80 steel begins to transform into austenite at  $713^{\circ}C$  ( $Ac_1$ ) and completes the transformation to austenite at  $880^{\circ}C$  ( $Ac_3$ ) in the heating process in Fig. 1. According to these values, the specimens whose peak temperatures are  $650^{\circ}C$  or  $780^{\circ}C$  experience only ferrite re-crystallization or local austenization. Thus, almost no difference can be seen between the OM image of the BM microstructure and the images of the SHAZ, CGHAZ and SCGHAZ microstructures because of the relatively low peak temperature (below  $Ac_1$ ). However, the micro-hardnesses of the SHAZ and SCGHAZ are obviously lower than those of the BM and CGHAZ, which can be attributed to the tempering-like treatment [19].

The microstructure of the ICHAZ still consists of PF and M/A constituents with finer grain sizes than those in the BM (Fig. 3b). However, the M/A constituents in the prior austenite grain boundaries and the GB grain boundaries grew substantially, showing a necklace-shape in the ICCGHAZ, which is very different from those boundaries in the CGHAZ (Fig. 4b). Previous studies have demonstrated that the ductility and toughness of the welded joint will decrease dramatically

because of the coarse necklace-shaped M/A constituents [7, 10]. The formation of the necklace-shaped microstructure results from complex processes. First, the coarse prior austenite grain boundaries and GB lath boundaries in the CGHAZ give the non-equilibrium microstructure a high degree of tropism. In addition, in the heating process of the ICCGHAZ samples, localized austenization occurs because the peak temperature is between  $Ac_1$  and  $Ac_3$ . More importantly, the transformation from  $\alpha$ -Fe to  $\gamma$ -Fe mainly occurs on the coarse prior austenite grain boundaries and the GB lath boundaries. Carbon atoms can diffuse to the reverted structure-coarse prior austenite grain boundaries and the GB lath boundaries. According to the Arrhenius equation, the diffusion rate of carbon atoms can be calculated as follows [6]:

$$D = D_0 \exp\left(\frac{-Q}{RT}\right) \quad (3)$$

where  $D_0$  is the initial diffusion rate of carbon atoms and equals  $6.2 \times 10^{-7} \text{ m}^2 \text{ s}^{-1}$ ,  $Q$  is the activation energy of diffusion and equals  $80 \text{ kJ mol}^{-1}$ ,  $T$  is the absolute temperature, and  $R$  is the ideal gas constant. Thus, the carbon atom diffusion rate,  $D$ , was calculated to be  $3.6 \times 10^{-11} \text{ m}^2 \text{ s}^{-1}$  at  $713 \text{ }^\circ\text{C}$  and  $6.7 \times 10^{-11} \text{ m}^2 \text{ s}^{-1}$  at  $780 \text{ }^\circ\text{C}$ .

The carbon atom diffusion distance,  $X_{3D}$ , can be calculated as follows:

$$X_{3D} = (6Dt)^{1/2} \quad (4)$$

where  $t$  is the time maintained spent at a given temperature.

The time maintained above  $Ac_1$  during the GMAW thermal cycles is 2.1 s according to Fig. 1. Subsequently,  $X_{3D}$  was calculated to be 21.3–28.9  $\mu\text{m}$ , which means that the carbon atoms can diffuse from the center of the prior austenite grains to the grain boundaries to make the reverted microstructure rich in carbon. In addition, martensite with a high carbon concentration can then be produced in the transformation of  $\gamma$ -Fe to  $\alpha$ -Fe in the cooling process. The bright-field image of the M/A constituents and corresponding indexed selected area electron diffraction (SAED) pattern are shown in Fig. 6. The size of the M/A constituents is approximately 2  $\mu\text{m}$ . Clearly, martensite twin crystals are present, which are indexed in Fig. 6b, and the twin crystal axis is [112]. The highest micro-hardness occurs in the ICCGHAZ, which can be attributed to the generation of high-carbon martensite.

The microstructure of the SCGHAZ with the peak temperature of  $950 \text{ }^\circ\text{C}$  is still mainly PF and M/A constituents with finer grains than those in the BM, which is beneficial for the mechanical properties according to the Hall-Petch relation [20] (Fig. 5c). In addition, the granular M/A constituents are distributed more uniformly than those in the BM. However, the microstructure of the SCCGHAZ is much coarser than that of the SCHAZ because of the inheritance effect, but much finer than that of the CGHAZ because of the recrystallization effect. In the SCCGHAZ, the M/A constituents are granular or strip-shaped.

The microstructures of CGHAZ-1 and UCGHAZ-1, CGHAZ-2 and UCGHAZ-2 are similar except that the prior austenite grain grew substantially in UCGHAZ-1 and UCGHAZ-2 because of the heredity effect. In CGHAZ-2 and UCGHAZ-2, the bainitic lath is much thinner, the M/A constituents are continuous and thinner, and the content of M/A constituents is higher than in the CGHAZ, which can be attributed to the high cooling rate in the GMAW thermal cycle.

For the HAZs that experienced only the GMAW cycles, the micro-hardness curve exhibits a “V” shape. The highest and lowest micro-hardness points respectively occur in the CGHAZ with a

high peak temperature and in the ICHAZ with a peak temperature between  $Ac_1$  and  $Ac_3$ . However, for the reheated CGHAZ samples that experienced the SAM+GMAW cycles, the micro-hardness curve exhibits a “W” shape. The highest micro-hardness point occurs in the ICCGHAZ with a secondary peak temperature between  $Ac_1$  and  $Ac_3$ . At other peak temperatures, the micro-hardnesses of the HAZ samples with only one welding thermal cycles are higher than those of the samples subjected to two welding thermal cycles because of the coarse microstructure of the former. These results are in accordance with the microstructure.

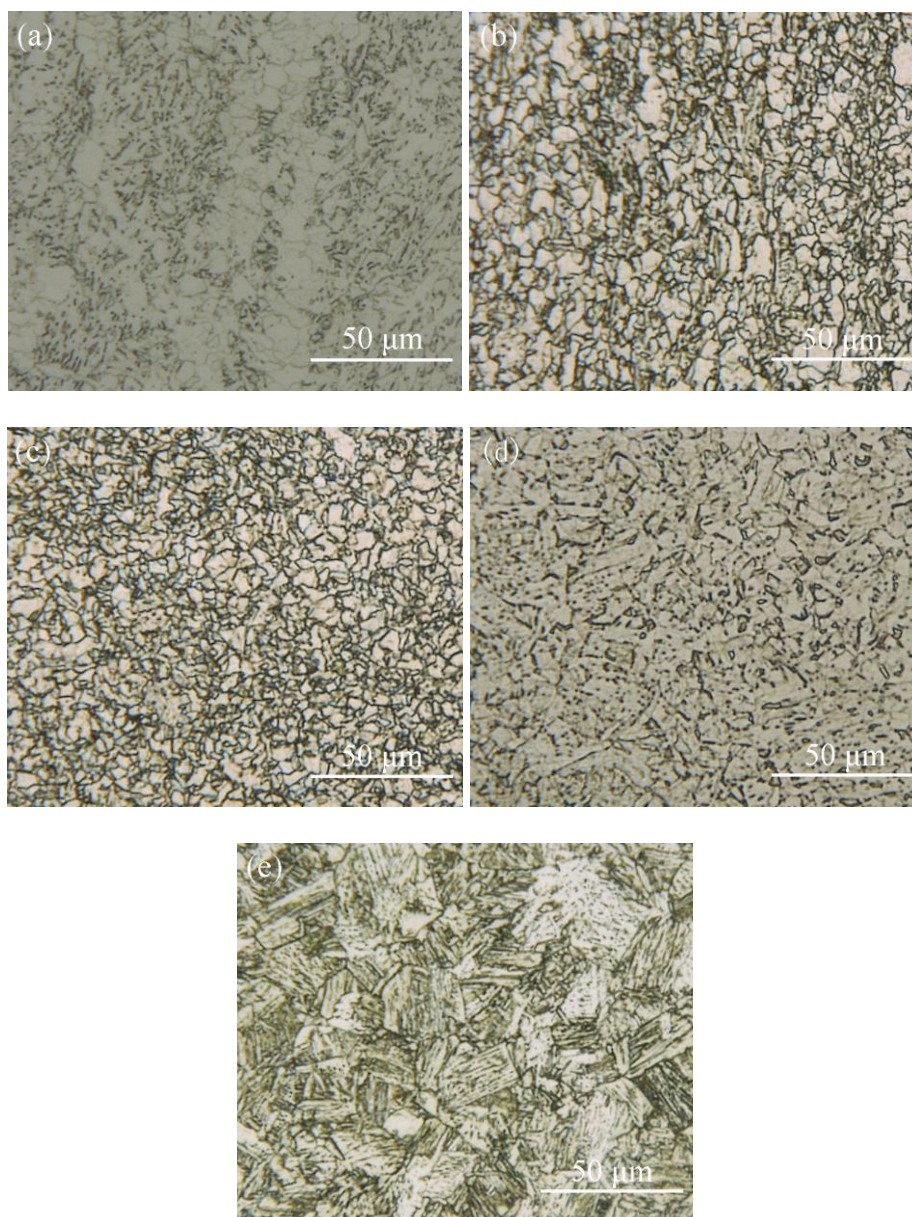


**Figure 3.** OM images of the microstructures of the HAZ samples experiencing only the GMAW thermal cycle: (a) SHAZ; (b) ICHAZ; (c) SCHAZ; (d) CGHAZ-1 and (e) CGHAZ-2.

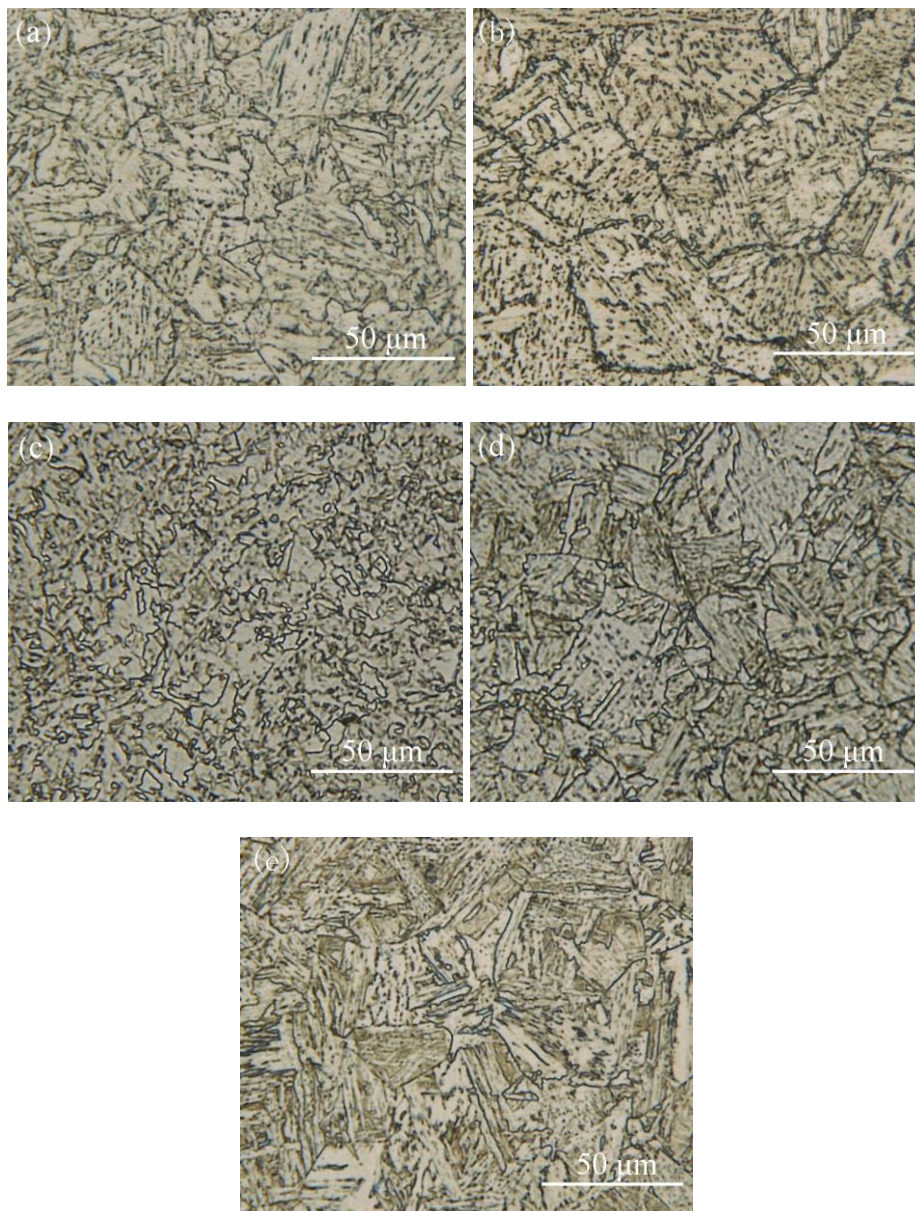


**Figure 4.** OM images of the microstructures of the HAZ samples experiencing the SAW+GMAW thermal cycle: (a) SCGHAZ; (b) ICCGHAZ; (c) SCCGHAZ; (d) UCGHAZ-1 and (e) UCGHAZ-2.

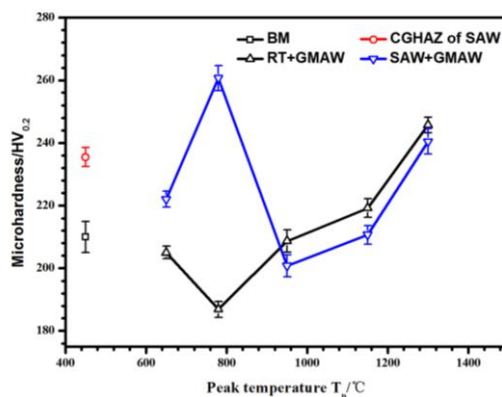


**Figure 5.** Effects of the welding thermal cycles on the microhardness of the HAZ samples experiencing RT+GMAW and SAW+GMAW thermal cycles.

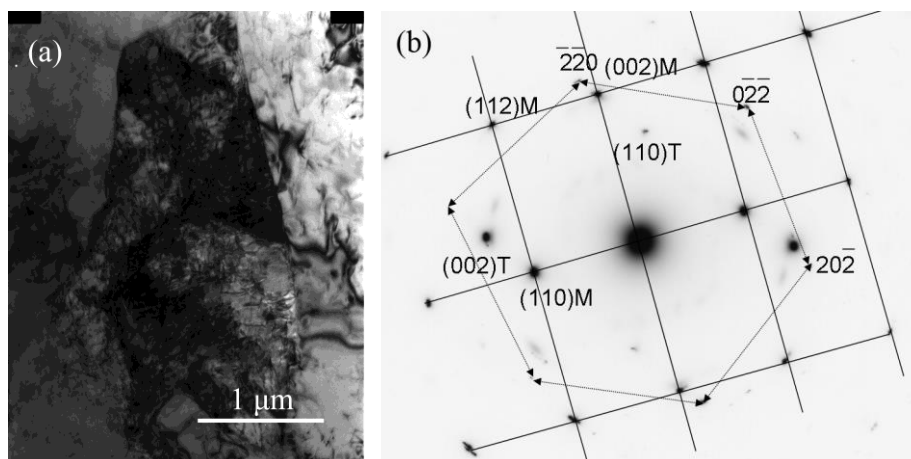


**Figure 6.** TEM images of the M/A constituents in ICCGHAZ: (a) bright-field image of the M/A constituents and (b) the corresponding indexed SAED pattern.

**Table 2.** Microstructural characteristics of the BM and HAZs

	Main matrix	Lath width ( $\mu\text{m}$ )	Prior austenite grain size ( $\mu\text{m}$ )	M/A constituents	
				Shape	Fraction (%)
BM	PF+GB	--	--	granular	15.9
CGHAZ	GB	1.21	28.1	granular	14.4
SHAZ	PF+GB	--	--	granular	15.9
ICHAZ	PF+GB	--	--	granular	16.3
SCHAZ	PF+GB	--	--	granular	17.7
CGHAZ-1	GB	--	--	granular	10.3
CGHAZ-2	BF	--	27.6	granular/needle-like	10.1
SCGHAZ	GB	1.21	28.1	granular	14.4
ICCGHAZ	GB	--	31.1	granular/massive	22.1
SCCGHAZ	GB+PF	--	--	granular/strip-shaped	15.4
UCGHAZ-1	BF	--	17.6	granular/needle-like	17.8
UCGHAZ-2	BF	0.75	41.2	needle-like	19.1

### 3.2 Corrosion behavior in a $\text{CO}_2$ environment

#### 3.2.1 Corrosion rate

The corrosion rates of different samples in 5.0 wt.% NaCl with saturated  $\text{CO}_2$  are shown in Fig. 7. The corrosion rates strongly depend on the microstructure, which is determined by the applied welding thermal cycles. As the immersion process proceeds, the corrosion rates of the BM, SHAZ, ICHAZ, SCHAZ and SCCGHAZ decrease, whereas those of the CGHAZ, CGHAZ-1, CGHAZ-2, SCGHAZ, ICCGHAZ, UCGHAZ-1 and UCGHAZ-2 increase. In addition, the corrosion rates of the SAW-GMAW HAZs are much higher than those of the RT-GMAW HAZs with the same peak temperature in the GMAW thermal cycles. Among the RT-GMAW HAZs, the corrosion rate of CGHAZ-2 is the highest, and that of the SCHAZ is the lowest and is even lower than that of the BM.

However, the corrosion rate of the ICCGHAZ is the highest and is approximately seven times of that of the BM, whereas the corrosion rate of the SCCGHAZ is the lowest among the SAW+GMAW HAZs. Among all samples, the corrosion rate of the ICCGHAZ is the highest.

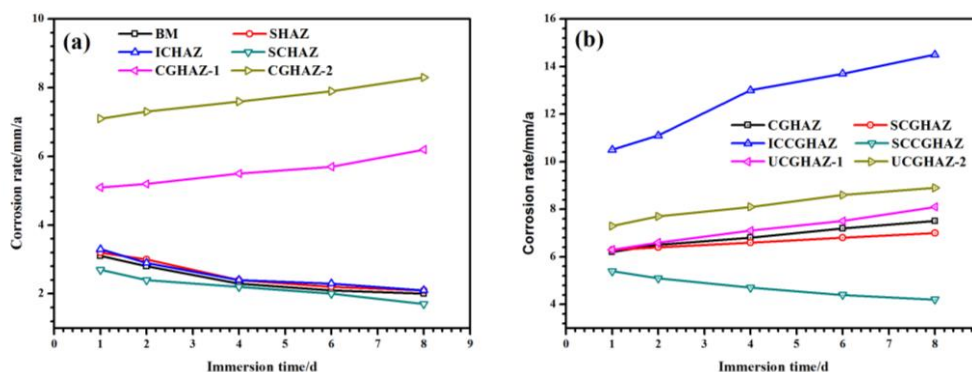


**Figure 7.** Corrosion rates of the BM and HAZs experiencing different welding thermal cycles in a 5.0 wt.% NaCl solution with saturated CO<sub>2</sub>: (a) the BM and RT+GMAW HAZs and (b) the CGHAZ and SAW+GMAW HAZs.

### 3.2.2 Open circuit potentials

The OCP of the different samples changes with the immersion time because of the changes that occur in the surface state (Fig. 8). The current density distribution and corrosion rate of each zone are unpredictable when the entire welded joint with a microstructural gradient is immersed in the solution because of the occurrence of the galvanic effect in the welded joint. However, the data for the individual immersion processes still possess reference value. As the immersion time increases, the OCPs of the BM, SHAZ, ICHAZ, SCHAZ and SCCGHAZ increase, and those of the CGHAZ, CGHAZ-1, CGHAZ-2, SCGHAZ, ICCGHAZ, SCCGHAZ, UCGHAZ-1 and UCGHAZ-2 decrease. The BM has a more positive potential than all the HAZs except the SCHAZ, indicating that the driving force for corrosion in the BM is lower than that in all the HAZs except the SCHAZ. For the HAZs, the SAW+GMAW HAZs have more negative potentials than the RT+GMAW HAZs for the same peak temperature in the GMAW thermal cycles, indicating that the driving force of the former is higher. Among the RT-GMAW HAZs, the OCP of CGHAZ-2 is the most negative, and that of the SCHAZ is the most positive. However, among the SAW+GMAW HAZs, the OCP of the ICCGHAZ is the most negative, and that of the SCCGHAZ is the most positive. In addition, the ICCGHAZ has the most negative OCP among all the samples, indicating that its corrosion driving force is the highest. These results support that the galvanic effect can be introduced because of the differences in the OCPs. Furthermore, the zones with a negative OCP act as anodes and are preferentially attacked when immersed in the electrolyte together [21], indicating that the ICCGHAZ is the weakest zone.

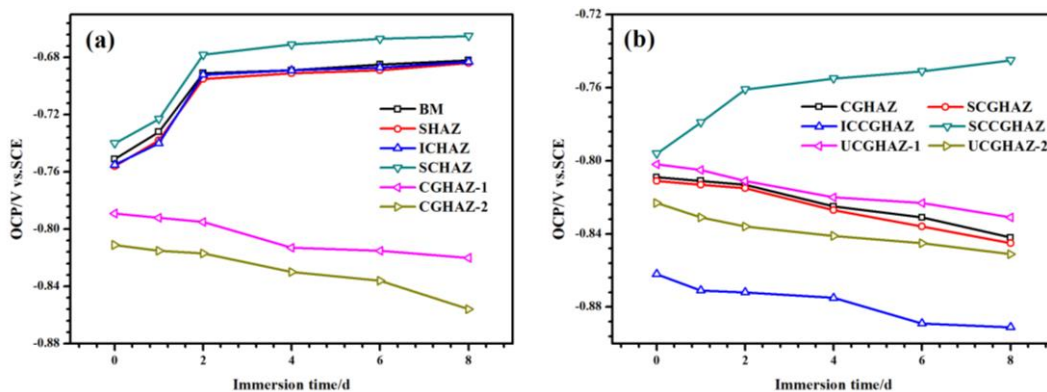


**Figure 8.** OCPs of different samples in a 5.0 wt.% NaCl solution with saturated CO<sub>2</sub>: (a) the BM and RT+GMAW HAZs and (b) the CGHAZ and SAW+GMAW HAZs.

### 3.2.3 Electrochemical impedance spectroscopy

The EIS results at the OCP, presented as Nyquist impedance diagrams, for the BM and simulated HAZs after immersion for 1, 2, 4, 6 and 8 days mainly show two styles (Fig. 9). In the initial immersion for 1, 2 and 4 days, the Nyquist impedance diagrams show a common feature of containing one capacitive loop in the high frequency region and one inductive loop in the low frequency region. However, differences are observed after immersion of 6 and 8 days. For the CGHAZ, CGHAZ-1, CGHAZ-2, SCGHAZ, ICCGHAZ, UCGHAZ-1 and UCGHAZ-2, the Nyquist plots after immersion for 6 and 8 days still contain one capacitive loop and one inductive loop. However, for the BM, SHAZ, ICHAZ, SCHAZ, and SCGHAZ, the inductive loop disappeared, and the radius of the capacitive loop increased dramatically in the Nyquist plots.

An equivalent circuit of  $R_s(Q_{dl}(R_{ct}(Q_f R_f)(LR_L)))$  (Fig. 10a), was chosen to analyze the EIS spectra of the samples containing one capacitive loop and one inductive loop in the Nyquist plot. In addition, an equivalent circuit of  $R_s(Q_{dl}(R_{ct}(Q_f R_f)))$  (Fig. 10b) was chosen to analyze the EIS spectra of the samples containing only one capacitive loop in the Nyquist plot. In these equivalent circuits,  $R_s$  is the solution resistance,  $Q_{dl}$  is the double layer constant phase element (CPE),  $R_{ct}$  is the charge transfer resistance,  $Q_f$  is the corrosion product film CPE,  $R_f$  is the corrosion product film resistance,  $L$  is the inductive reactance and  $R_L$  is the inductive reactance resistance. The fitting results of  $R_{ct}$ , the representative of corrosion resistance, and  $R_f$ , the representative of the protectiveness of the corrosion product film, are shown in Figs. 11 and 12. The values of  $R_{ct}$  and  $R_f$  are consistent with the size of the capacitive loop in the Nyquist plots. The  $R_{ct}$  and  $R_f$  values of the SAW+GMAW HAZs are lower than those of the RT+GMAW HAZs for the same peak temperature in the GMAW thermal cycle. There are clearly two sets of regular changes in the  $R_{ct}$  and  $R_f$  values.

The  $R_{ct}$  and  $R_f$  values of the BM, SHAZ, ICHAZ, SCHAZ and SCCGHAZ increased to thousands of  $\Omega \text{ cm}^2$ , and the rate of increase gradually, increased as the immersion process proceeded. However, those of the CGHAZ, CGHAZ-1, CGHAZ-2, SCGHAZ, ICCGHAZ, UCGHAZ-1 and UCGHAZ-2 decreased after the immersion process, although the attenuation range was small. Among the RT-GMAW HAZs, the  $R_{ct}$  and  $R_f$  values of CGHAZ-2 are the lowest, and those of the SCHAZ are

the highest. However, the  $R_{ct}$  and  $R_f$  values of the ICCGHAZ are the lowest and those of SCCGHAZ are the biggest among the SAW+GMAW HAZs. In addition, the  $R_{ct}$  and  $R_f$  values of the ICCGHAZ are the lowest among all the samples, indicating that it is the weakest zone of corrosion resistance, which is in accordance with the corrosion rate and the OCP results.

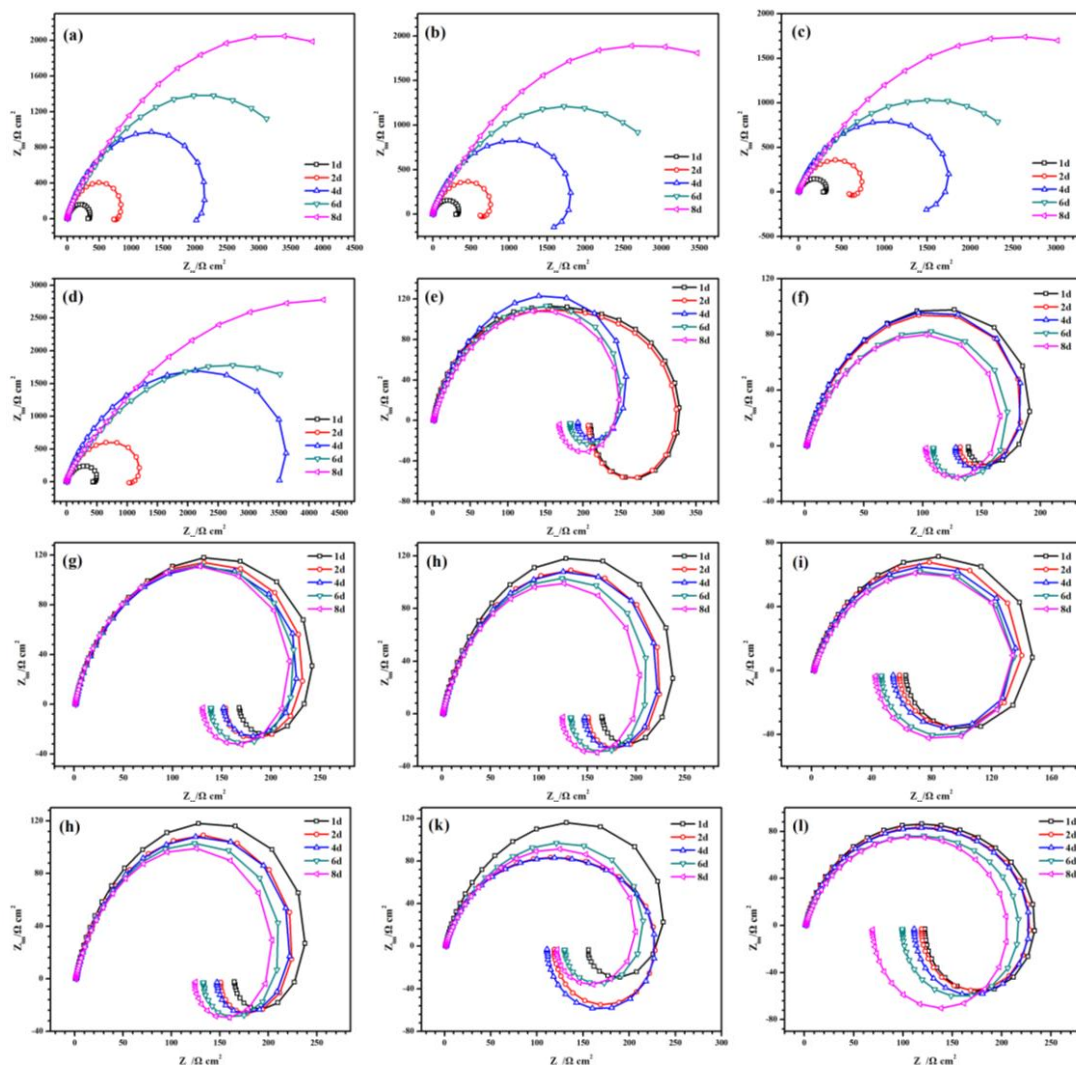


**Figure 9.** Nyquist plots of the BM and HAZ samples in a 5.0 wt.% NaCl solution with saturated CO<sub>2</sub>: (a) BM; (b) SHAZ; (c) ICHAZ; (d) SCHAZ; (e) CGHAZ-1; (f) CGHAZ-2; (g) CGHAZ; (h) SCGHAZ; (i) ICCGHAZ; (j) SCCGHAZ; (k) UCGHAZ-1 and (l) UCGHAZ-2.

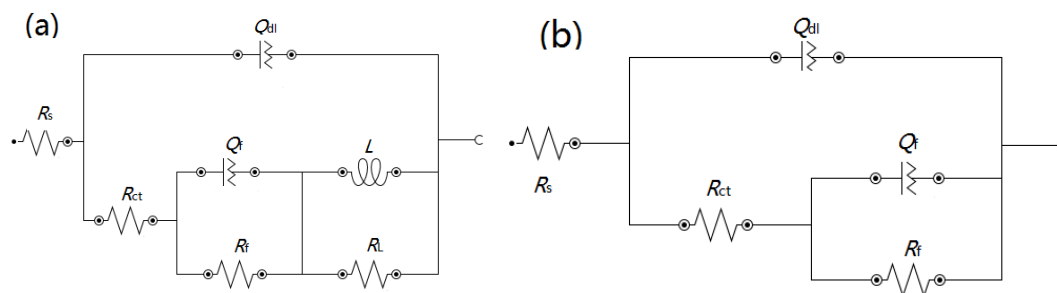


**Figure 10.** Equivalent circuits of  $R_s(Q_{dl}(R_{ct}(Q_f R_f)(LR_L)))$  and  $R_s(Q_{dl}(R_{ct}(Q_f R_f)))$ : (a)  $R_s(Q_{dl}(R_{ct}(Q_f R_f)(LR_L)))$  and (b)  $R_s(Q_{dl}(R_{ct}(Q_f R_f)))$

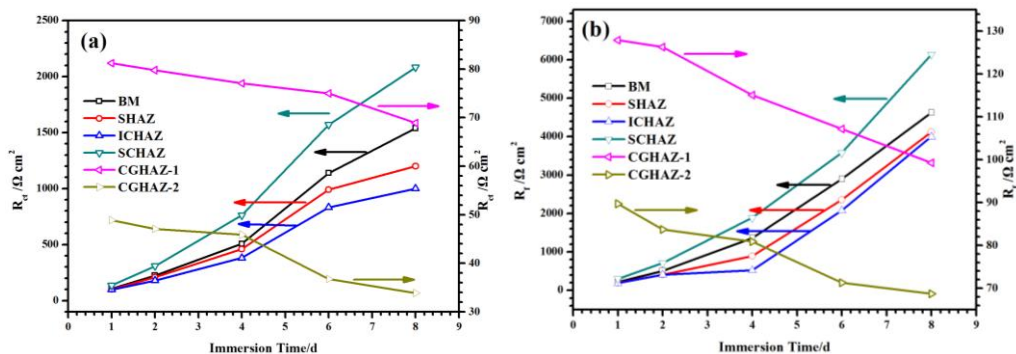


Figure 11. Fitting results of the  $R_{ct}$  and  $R_f$  values of the BM and RT+GMAW HAZs: (a)  $R_{ct}$  and (b)  $R_f$ .

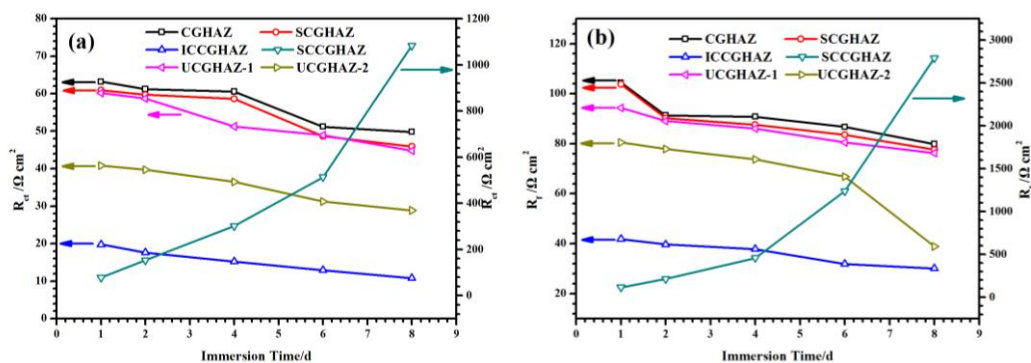
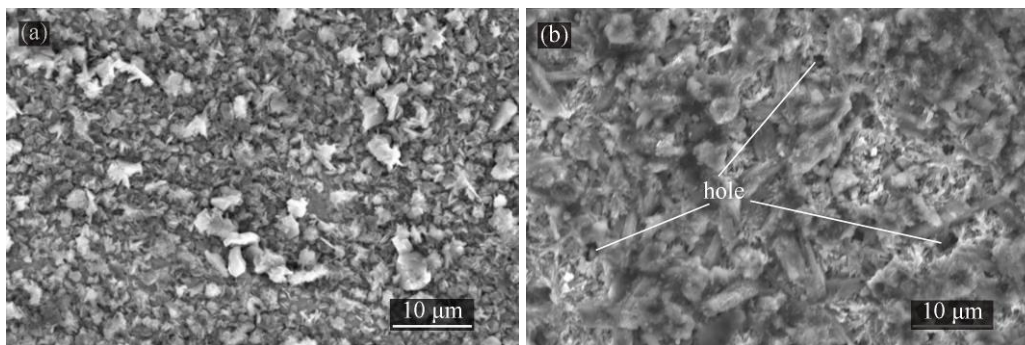
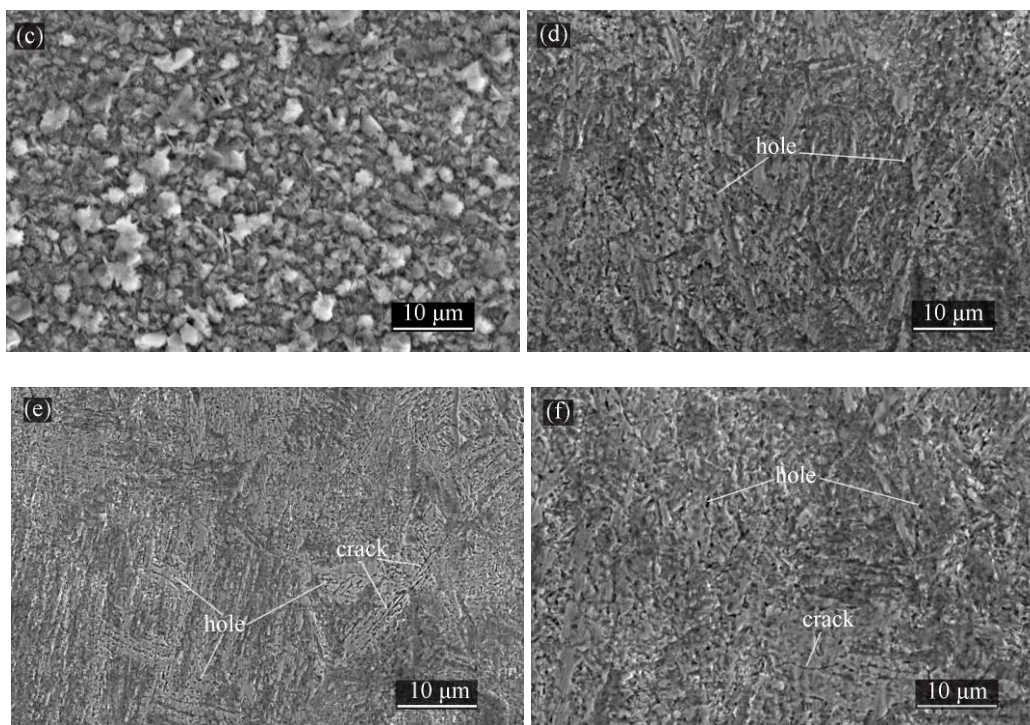


Figure 12. Fitting results of the  $R_{ct}$  and  $R_f$  values of the CGHAZ and SAW+GMAW HAZs: (a)  $R_{ct}$  and (b)  $R_f$ .

### 3.2.4 Corrosion morphologies

The steel surface morphologies after immersion for 8 days are shown in Fig. 13. A fairly dense, fine and perfect layer of corrosion products several microns thick and containing some nanoscale holes was generated on the BM surface (Fig. 13a).





**Figure 13.** Corrosion morphologies after immersion for 8 days in 5.0 wt.% NaCl with saturated CO<sub>2</sub>: (a) BM, (b) ICHAZ, (c) SCHAZ, (d) CGHAZ-2, (e) ICCGHAZ and (f) UCGHAZ-2.

The corrosion product film contributes to the significant increase observed in the corrosion resistance of the BM during the immersion process. Similar results were observed for the SCHAZ surface (Fig. 13b), in which the corrosion product layer was thinner than that on the BM.

However, many small holes are present on the surfaces of the CGHAZ, ICCGHAZ and UCGHAZ-2 as a result of the poor adherence of the deposited products to the surface, forming a honeycombed surface. In addition, some micron-sized cracks can be seen on the surfaces of the ICCGHAZ and UCGHAZ-2.

## 4. DISCUSSION

### 4.1 Reaction mechanisms

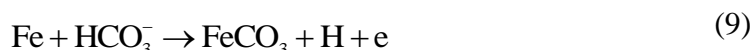
According to previous studies, during the first stage of corrosion, the anodic reaction is the oxidation of iron. In addition, FeOH and FeOH<sup>+</sup> are formed as intermediate products as follows [22]:



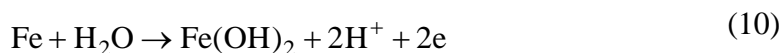
During the corrosion of steel, ferrous carbonate can form and deposit on the steel surface when the concentration of Fe<sup>2+</sup> reaches saturation [23]:



In addition, ferrous carbonate can be formed through the oxidation of Fe, as follows [13]:



Moreover, ferrous hydroxide can be formed at the same time through the oxidation of Fe, as follows:



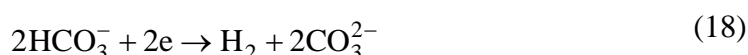
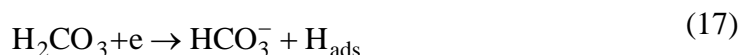
Ferrous hydroxide can be transformed to ferrous carbonate when the pH is relatively high, as follows [24]:



However, the cathodic reactions between the steel and 5.0 wt.% NaCl with saturated CO<sub>2</sub> are complex. First, the preparation reactions of the dissolution and adsorption of CO<sub>2</sub> and the ionization of H<sub>2</sub>CO<sub>3</sub> occur at the cathode, as follows :



The reactants of the cathodic reactions, such as H<sup>+</sup>, H<sub>2</sub>CO<sub>3</sub> and HCO<sub>3</sub><sup>-</sup>, are produced in the preparation reactions. The cathodic reactions are the reduction of H<sup>+</sup>, H<sub>2</sub>CO<sub>3</sub> and HCO<sub>3</sub><sup>-</sup>, as follows [25, 26]:



#### 4.2 Corrosion mechanisms of the different samples

The results of the corrosion rate, electrochemistry and corrosion morphology are consistent, indicating that the effects of the welding thermal cycles on the corrosion behavior and resistance are complex and important because of the complex microstructural gradients formed in the welded joint. Furthermore, the findings are in accordance with those from previous studies [2, 4, 13, 14, 19, 27, 28].

The corrosion resistance of the BM is superior to that of all the HAZs except the SCHAZ because of the coarse microstructure and presence of residual welding stress in the HAZs. This result is similar to the results of the corrosion resistance in a H<sub>2</sub>S environment [21].

The corrosion resistances of the HAZs that experienced the SAW-GMAW thermal cycle are inferior to those of the HAZs that experienced only the GMAW thermal cycle with the same peak temperature because of the relatively coarse microstructure of the former group of samples. CGHAZ-2 with a peak temperature of 1300 °C is the weakest zone among the HAZs not experiencing the second thermal cycles. However, the ICCGHAZ with a peak temperature of 780 °C, which is between Ac<sub>1</sub> and Ac<sub>3</sub>, is the weakest zone among all the HAZs because of the presence of necklace-shaped coarse M/A constituents. Previous studies have shown that the presence of a necklace-shaped microstructure can

lower the mechanical properties [5, 7, 10, 21, 29]. A subsequent heat treatment may enhance both the corrosion resistance and the mechanical properties of the ICCGHAZ by eliminating the necklace-shaped microstructure [30]. Further research on the effects of heat treatment on the corrosion resistance should be completed in the near future.

Previous studies have shown that differences in the microstructure can cause different corrosion morphologies to form [28]. The two different sets of corrosion morphologies (Fig. 13) contribute to the two sets of regular changes observed in the corrosion resistance (Fig. 8-12), especially during immersion for more than 4 days. The deposition of the corrosion products on some of the sample surfaces clearly results in increases in the OCP,  $R_{ct}$  and  $R_f$  [31]. In addition, it can be concluded that the corrosion products are difficult to deposit on the steel surface and that the corrosion resistance decreases as the immersion progress proceeds, if the prior austenite grain boundaries can be seen clearly, as in the CGHAZ-1, CGHAZ-2, SCGHAZ, ICCGHAZ, UCGHAZ-1 and UCGHAZ-2.

The orders of corrosion and dissolution of the different phases or microstructures in corrosive environments are different. The vulnerability of ferrite has been shown to be higher than that of  $Fe_3C$ , and a passive film is formed that transforms into the  $Fe_3C$  phase [32-34]. Martensite is a kind of non-equivalent microstructure with a high carbon concentration and high micro-hardness that is present in the M/A constituents. This structure, especially high-carbon martensite, has a high potential to preferentially dissolve in the electrolyte, producing a hole on the steel surface. In addition, the corrosion products of  $FeCO_3$  or  $Fe(OH)_2$  deposit on the other zones. Thus, the galvanic effect could then occur between the hole regions and the corrosion products that cover certain regions. The galvanic effect would contribute to localized corrosion [18] and pitting, which has been demonstrated by the presence of an inductive loop in the EIS results of every sample during the initial immersion period and by the pitting observed on the steel surface in Fig. 13.

In addition, the extent of the preferential dissolution of martensite strongly depends on the galvanic effect between the M/A constituents and the nearby zones. In turn, the galvanic effect depends on the differences in the zones, including the size, shape and distribution of M/A constituents. In the CGHAZ and the reheated CGHAZ, the galvanic effect is relatively strong because of their high length/width ratios, high area ratio and high carbon concentrations. Thus, the M/A constituents have a high potential to preferentially dissolve and a low corrosion resistance. In addition, a large amount of reaction heat was released, and the corrosion products that had formed on the steel surface fell off under the action of internal stress and reaction heat, as shown in Fig. 13d-f. The presence of an impedance loop in the test of the whole CGHAZ and reheated CGHAZ was attributed to this phenomenon. However, the reaction with the electrolyte was not as acute for the BM and the other HAZs. Thus, the corrosion products could deposit on the steel surface to form a corrosion product film. Furthermore, the high carbon concentration, residual welding stress and lattice distortion of martensite in the M/A constituents of ICCGHAZ resulted in more pitting and a low corrosion resistance, making it the weakest zone.

## 5. CONCLUSIONS

Different microstructural gradients were formed in the BM and the CGHAZ after experiencing the same SAW thermal cycle of 10 kJ/cm, and the  $CO_2$  corrosion behaviors was studied for each zone.

The corrosion resistance of the BM was shown to be superior to that of all the HAZs except the SCHAZ because of the coarse microstructure and the presence of residual welding stress in the HAZs. The corrosion resistances of the SAW+GMAW samples were inferior to those of the RT+GMAW samples with the same peak temperature, which can be attributed to the relatively coarse microstructure of the former. The preferential dissolution of the M/A constituents contributed to the presence of pitting and produced an inductive loop in the Nyquist plots and holes in the corrosion morphologies in some of the sample surfaces. More importantly, the corrosion resistance of the ICCGHAZ was the weakest because of the presence of coarse necklace-shaped M/A constituents containing high-carbon martensite.

#### ACKNOWLEDGMENTS

The authors are greatly appreciative of the support of the Natural Science Foundation of Shandong Province IN China (No.ZR2016EEB31)

#### References

1. H.B. Xue and Y.F. Cheng, *Electrochim. Acta*, 55 (2010) 5670.
2. S. Bordbar, M. Alizadeh and S.H. Hashemi, *Mater. Design*, 45 (2013) 597.
3. Y.D. Han, H.Y. Jing and L.Y. Xu, *Mater. Chem. Phys.*, 132 (2012) 216.
4. F. Mohammadi, F.F. Eliyan and A. Alfantazi, *Corros. Sci.*, 63 (2012) 323.
5. V.G. Haugen, B.R.S. Rogne, O.M. Akselsen, C. Thaulow and E. Østby, *Mater. Design*, 59 (2014) 135.
6. X. Li, X. Ma, S.V. Subramanian, C. Shang and R.D.K. Misra, *Mat. Sci. Eng. A-Struct.*, 616 (2014) 141.
7. Z. Zhu, L. Kuzmikova, H. Li and F. Barbaro, *Mat. Sci. Eng. A-Struct.*, 605 (2014) 8.
8. S. Kim, D. Kang, T.W. Kim, J. Lee and C. Lee, *Mat. Sci. Eng. A-Struct.*, 528 (2011) 2331.
9. Y. You, C. Shang, L. Chen and S. Subramanian, *Mater. Design*, 43 (2013) 485.
10. X. Li, Y. Fan, X. Ma, S.V. Subramanian and C. Shang, *Mater. Design*, 67 (2015) 457.
11. W.C. Zhu, W.H. Leng, J.Q. Zhang and C.N. Cao, *Acta Metall. Sin. Engl.*, 19 (2006) 91.
12. Z. Liu, X. Li, Y. Zhang, C. Du and G. Zhai, *Acta Metall. Sin. Engl.*, 22 (2009) 58.
13. G.A. Zhang and Y.F. Cheng, *Corros. Sci.*, 51 (2009) 1714.
14. G.A. Zhang and Y.F. Cheng, *Electrochim. Acta*, 55 (2009) 316.
15. F.F. Eliyan and F. Mohammadi, A. Alfantazi, *Corros. Sci.*, 64 (2012) 37.
16. G.A. Zhang, N. Yu, L.Y. Yang and X.P. Guo, *Corros. Sci.*, 86 (2014) 202.
17. M. Honarvar Nazari, S.R. Allahkaram and M.B. Kermani, *Mater. Design*, 31 (2010) 3559.
18. G.A. Zhang and Y.F. Cheng, *Electrochim. Acta*, 56 (2011) 1676.
19. L.W. Wang, Z.Y. Liu, Z.Y. Cui, C.W. Du, X.H. Wang and X.G. Li, *Corros. Sci.*, 85 (2014) 401.
20. C.F. Dong, X.G. Li, Z.Y. Liu and Y.R. Zhang, *J. Alloys Compd.*, 484 (2009) 966.
21. W. Zhao, Y. Zou, K. Matsuda and Z. Zou, *Mater. Design*, 99 (2016) 44.
22. M.A. Islam and Z.N. Farhat, *Tribol. Int.*, 68 (2013) 26.
23. B.R. Linter and G.T. Burstein, *Corros. Sci.*, 41 (1999) 117.
24. Z.D. Cui, S.L. Wu, S.L. Zhu and X.J. Yang, *Appl. Surf. Sci.*, 252 (2006) 2368.
25. Y. Zhang, X. Pang, S. Qu, X. Li and K. Gao, *Int. J. Greenhouse Gas Control*, 5(2011) 1643.
26. J. Han, J. Zhang and J.W. Carey, *Int. J. Greenhouse Gas Control*, 5(2011) 1680.
27. F.F. Eliyan and A. Alfantazi, *Corros. Sci.*, 74 (2013) 297.
28. M. Alizadeh and S. Bordbar, *Corros. Sci.*, 70 (2013) 170.
29. E. Bonnevie, G. Ferrière, A. Ikhlef, D. Kaplan and J.M. Orain, *Mat. Sci. Eng. A-Struct.*, 385 (2004) 352.

30. X.L. Wang, X.M. Wang, C.J. Shang and R.D.K. Misra, *Mat. Sci. Eng. A-Struct.*, 649 (2016) 282.
31. W. Zhao, Y. Zou, K. Matsuda and Z. Zou, *Corros. Sci.*, 102 (2016) 455.
32. F.F. Eliyan and A. Alfantazi, *Corros. Sci.*, 74 (2013) 297.
33. P. Bai, H. Zhao, S. Zheng and C. Chen, *Corros. Sci.*, 93 (2015) 109.
34. H.H. Huang, W.T. Tsai and J.T. Lee, *Electrochim. Acta*, 41 (1996) 1191.

© 2018 The Authors. Published by ESG ([www.electrochemsci.org](http://www.electrochemsci.org)). This article is an open access article distributed under the terms and conditions of the Creative Commons Attribution license (<http://creativecommons.org/licenses/by/4.0/>).